Anisotropic and hyperelastic mechanical response of 3D printed TPU parts

---

Abstract

Thermoplastic polyurethane (TPU) is usually considered isotropic and hyperelastic. Nevertheless, when 3D printing techniques as Fused Deposition Modeling (FDM) are used, an anisotropic behaviour (inherent to the process) is expected. The aim of the present research is to analyse the isolated effect of the raster angle on the mechanical response of 3D printed TPU parts. To avoid other effects, several specimens were manufactured with 100% infill density and parallel straight lines infill pattern. Four different printing configurations were analysed, 0°, ±45°, 90° and concentric pattern. The specimens were subjected to tensile loading and obtained data was used as input to fit three hyperelastic behaviour models, specifically the neo-Hookean, Ogden and Mooney-Rivlin models are compared. The obtained results show that the raster angles have a clear effect on the mechanical properties of the 3D printed parts, leading to an anisotropic behaviour of the obtained specimens and on the appearance of the different stages of the hyperelastic behaviour. In addition, the fitting models used allowed to conclude that the neo-Hookean model is the best fitting the initial linear-elastic zone, while for the whole stress-strain curve, both the Ogden and Mooney-Rivlin models produce very good approximations.

Keywords: 3D printing, ALM, hyperelastic, anisotropy, raster angle

---

1. Introduction

Additive manufacturing (AM) is becoming increasingly popular in many fields, ranging from everyday household items, to various mechanisms, to medical components and instruments, and is even used in the food industry. This growth has been possible because AM is capable of manufacturing a variety of materials, such as polymers, metals, natural fibres and ceramics [1]. There are different AM techniques such as stereolithography (SLA), which is a fast process with a good surface finish and the parts can be subsequently machined without any prior treatment. However, the parts obtained from this technique must be cured with ultraviolet light and the mechanical properties of these parts change over time, becoming increasingly fragile. Another technique is selective laser sintering (SLS), which produces parts with mechanical characteristics close to the final material. This technology is suitable for assemblies of parts that need to be assembled and disassembled. A disadvantage of this technique is that the obtained parts are porous and therefore require post-processing. In addition, these parts must be cleaned due to the powder residues that remain on their surfaces [2, 3]. Finally, Fused Filament Fabrication (FFF) also known as Fused Deposition Modelling (FDM), allows a wide variety of materials to be manufactured, such as ABS, PLA, TPU, PC, etc., as well as materials reinforced with fibres. No post-curing is required and it is the most economical AM technique, both in terms of material and equipment. However, detail levels are usually lower than other technologies and the temperature in the working area must be controlled [4]. Nevertheless, FDM is the most widely used in the literature because it is a rapid prototyping technology, which has led to the increasing use of thermoplastic and rubber materials in engineering applications, mainly due to their hyperelastic character, which gives them great deformation under load. Additionally, when these materials are unloaded, they recover their original shape with reduced permanent deformation. With this type of material, much lighter parts can be obtained.

Among the different thermoplastic materials and elastomers that can be used in FDM manufacturing, the most commonly used are poly lactic acid (PLA) and thermoplastic polyurethane (TPU) [5]. Although PLA can be considered a biodegradable material [6] and is currently widely used in FDM, its applications in industry are limited due to its low toughness and impact resistance that make it a brittle material [5, 7]. On the other hand, TPU has high abrasion resistance, high elongation, good tensile and compressive strength, as well as being a biocompatible material [8]. As a result, TPU has been increasingly used in many engineering applications in recent years, such as soft robotic components [9], shoe soles, tyres, inflatable structures, conveyor belts, artificial joints, coatings, adhesives and foams [6, 10].

That is why, more and more works are focused on characterising the behaviour of TPU as a function of different printing parameters, such as raster angle, infill pattern, infill density, printing temperature and speed, etc [6, 9, 10, 11, 12, 13, 14, 15]. Among these works, Cameron et al. [9], analysed how different printing parameters such as extrusion temperature, raster angle or air gaps affect the maximum axial stress supported by the specimens. For this purpose, tensile tests are carried out at a displacement rate of 10 mm/min according to ASTM D3039. The conclusions reached in that work are that the air gaps have a higher impact on the maximum breaking strain than the rest of the analysed properties. Other works, such as the one carried out by Nace et al. [11], analyse the influence of the infill pattern type on the mechanical response. In that work, different types of infill patterns are used, as well as different infill densities, and they were subjected to compression tests in accordance with ISO 3386-1. This work concluded that the infill density has a clear effect on the mechanical properties of the material, however, the effect of the infill pattern is more complex. Following the same line of the previous works, Xiao and Gao [12] analysed the orientation of the infill pattern and the printing temperature effect on the mechanical properties of the specimens. For this purpose, they design specimens with a grid-shaped infill pattern oriented at 0° and 45°, manufactured at different melting temperatures, and tested them under tensile loading at a speed of 500 mm/min. The authors concluded that the fusion temperature and the angle of the pattern have an effect on the mechanical properties, stating that the optimum combination is a raster angle of 45° and a fusion temperature of 215°C. The work of Bruère et al. [13] analysed the effect of infill deposition angle and contour lines on tensile behaviour and stress relaxation. The orientations and patterns are similar to those used in [12]. Tensile tests were performed according to ISO 37 and DIN 53504 S3A. From the obtained results, it can be concluded that the raster angle has a low influence at low strains and that stress relaxation is not affected by contour lines and raster angle. Boubakri et al. [10], analysed how the ageing of the filaments that forms the specimens manufactured by FDM affects the mechanical properties of the TPU. For this purpose, they carried out tensile tests on the specimens following the ISO 527-2 standard at a constant cross-head speed of 10 mm/min. This work concludes that ageing had a significant effect on the mechanical properties of the material. Finally, Marco et al. [16] introduced an infrared light powder bed fusion system able to improve the elongation of TPU parts. Other works studied the use of 3D printed TPU on different kind of applications as prostheses, dampers, stents, among others, see [17, 18, 19]. TPU is also used combined with other plastics as MPP or PLA using 3D printing techniques [20, 21, 22].

As can be seen, TPU is a polymer that has been widely studied in the literature, however, the number of studies using hyperelastic material models in this material is not widespread. This may be due to its flexibility, presenting hyperelastic and viscoelastic behaviour, with significant elastic deformation, which difficult this type of study. One of the works that uses hyperelastic material models for TPU is the one carried out by Dilibal et al [14]. In this study, a comparison is made between the experimental and numerical data of three soft pneumatic actuators made of TPU. Firstly, tensile tests were performed to obtain different hyperelastic material models such as the neo-Hookean model, the two-parameter Mooney-Rivlin model and the Ogden model. Subsequently, they subjected the soft pneumatic actuators to bending, concluding that the experimental and numerical data are very similar, although the best fitting model for bending is the Ogden model. In Raj et al. [15], they modelled the mechanical behaviour of a TPU and Thermoplastic Polyurethane-Carbon Nanotube composite material under compression. For this purpose, they used the two-parameter Mooney-Rivlin hyperelastic model and the Ogden model, and compared the results obtained with viscoelastic and hyper viscoelastic models. Finally, they concluded that for the tests carried out, the hyperelastic models provide the worst fit to the experimental data. In the work carried out by Abad et al. [23], a computational analysis of membranes made with different hyperelastic materials: latex, silicone, natural rubber and nitrile rubber is presented. The hyperelastic material models used in that work are the one-order Mooney-Rivlin model, the second-order Mooney-Rivlin model, the Yeoh model, the Ogden model of order three and the Arruda-Boyce model. The authors concluded that for latex and nitrile rubber, the best-fitting hyperelastic model is the second-order Mooney-Rivlin model. For natural rubber and silicone all models show good fitting.

From the hyperelastic fitting models cited above, the neo-Hookean model can achieve good fits in the linear-elastic zone of rubber-like materials [24]. The Mooney-Rivlin model [25, 26] is an extension of the neo-Hookean model, in which the accuracy is improved. Both the first-order (2-parameter) and second-order (5-parameter) models are widely used in the literature. The use of a second-order model would allow a better fitting of the double curvature that hyperelastic materials present in their stress-strain curve, but it involves solving a much more complex stress equation. Finally, the Ogden model [27] captures with a very good accuracy the stiffness behaviour of the stress-strain relationship for rubber-type materials. In contrast to the other models, it does not use invariants in its strain energy equation.

The previously described works highlight the importance that TPU is currently taking on. This motivates the two objectives of the present research. The first one is to verify if the raster angle causes an anisotropic behaviour as it does in other 3D printed materials, e.g. carbon fibre reinforced thermoplastics [28, 29]. To fulfil this objective a mechanical characterisation of 3D printed TPU parts as a function of the raster angle in uniaxial tensile tests is done. In contrast to other works, a line infill pattern and 100% infill density were used in this work to avoid any other possible effect on the expected anisotropic behaviour. The second objective focuses on a numerical analysis of the experimental data using the neo-Hookean, Mooney-Rivlin and Ogden models of hyperelastic material behaviour. Subsequently, they are compared in order to analyse which of the three models fit best the hyperelastic behaviour of the 3D printed TPU parts using the experimentally obtained data. An adequate characterisation of 3D printed TPU will help designers to have more accurate models of their designed parts.

2. Materials and method

2.1. Material and specimens

Thermoplastic polyurethane (TPU) was chosen to print the specimens. Experimental tensile tests were done following ISO 37 standard. This standard contains a method to determine the stress-strain parameters by means of uniaxial tensile loading on thermoplastic and vulcanised rubbers. This standard allowed the use of two types of specimens, dumbbell-shaped or ring-shaped specimen. In this work, the type 1, dumbbell-shaped, specimens were used, the shape and dimensions are shown in figure 1.

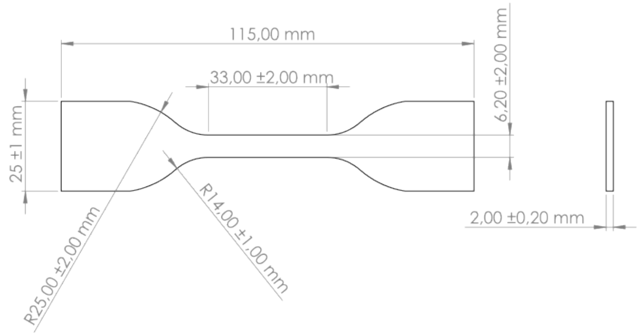

Figure 1: Test specimen type 1 shape and dimensions according to ISO37.

2.2. Printing process

From the different types of TPU available on the market, FLEX 93A TPU from Smart Materials® was chosen. The most interesting physical and mechanical properties are shown in the table 1.

Property	Value	Standard
Density	1.21 g/cm^3	ASTM D792
Tensile strength	12.7 MPa	ISO 527
Elongation at fracture traction	301.4%	ISO 527
100% elongation modulus	9.5 MPa	ISO 37
300% elongation modulus	19.5 MPa	ISO 37

Table 1: Physical and mechanical properties of the material used [30]

.

The specimens (Figure 1) were designed in the CAD software SolidWorks® and exported in .STL format. Then, the files were imported into Ultimaker Cura® slicer software version 5.3. This software allows to select the printer model from a database, as well as the material to be printed and the diameter of the extruder. The specimens were printed on an Artillery Genius Pro® printer with a bed of 220x220x250 mm. A 0.4 mm extruder and 1.75 mm filament diameter were used. In order to keep the test method consistent, all samples were printed from the same spool of material and with the same printing parameters, except for the raster angle of the infill pattern. The printing parameters used to produce the specimens are summarised in the table 2.

Table 2 also shows that the infill density used is 100% and the filling pattern is lines, since as mentioned previously, other variables that may affect the anisotropy are avoided. This table also reflects the fact that the specimens were manufactured without walls, base and top layers to avoid the modification of the overall mechanical properties of the specimen. In addition, when choosing these options, the specimens actual thickness may be affected. So, in order to comply with the standard, thickness measurements were taken at the centre and at each end of the test length of the specimen to ensure that none of these 3 measurements differed more than 2% from the median thickness.

The analysed infill configurations were obtained using different raster angles (Figure 2). These angles were 0° (Figure 2a), ±45° (Figure 2b) and 90° (Figure 2c). Additionally, a concentric line infill pattern was analysed (Figure 2d).

Parameters	Value	Units
Layer height	0.16	mm
Infill line width	0.44	mm
Wall thickness	0	mm
Top/Botton thickness	0	mm
Bottom layers	0	mm
Infill density	100	%
Printing temperature	228	°C
Build plate temperature	30	°C
Print speed	20	mm/s
Enable retraction	Yes	
Fan speed	100	%
Build plate adhesion type	Skirt	
Skirt line count	4	
Skirt distance	10.0	mm
Infill pattern	Lines	
Infill line distance	0.40	mm

Table 2: Most important printing parameters used to manufacture the specimens included in the slicing software Ultimaker Cura® version 5.3.

2.3. Equipment

The tensile tests were carried out on an Instron® 4483 series electromechanical machine. A 5 kN load cell was installed (Figure 3a). Additionally, an Instron® video extensometer model AVE 1 2663-821 (Figure 3b) was used to measure the strains during the test, using high-resolution cameras and initial marks with circular geometry on the specimens. The marking of the specimens, as well as the distance between marks, was carried out using a guide pattern provided by Instron® (Figure 3c). Before each test, the length of the initial distance between marks was automatically measured and used both for strain calculations and to eliminate errors introduced by inaccurate placement of the marks on the specimen.

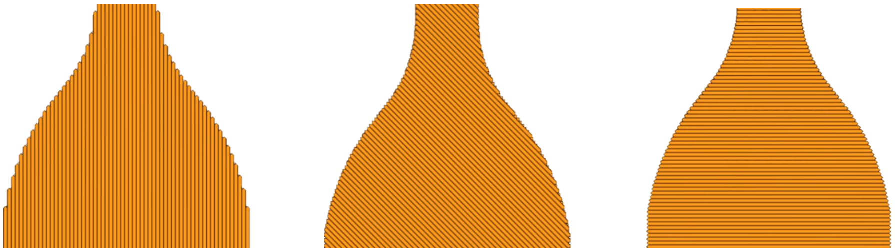

(a) 0°. (b) ±45°. (c) 90°.

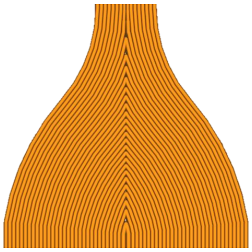

(d) Concentric.

Figure 2: Detail of the analysed configurations (different raster angles) on a printed layer. Each line corresponds to a deposited filament.

(a) (b) (c)

Figure 3: (a) Instron® 4483 machine during tensile test. (b) Video Extensometer. (c) Initial length marks on ±45° specimens.

The video extensometer is capable of absolute measurement, allowing it to obtain the extension in absolute units of displacement and strain percentage. In order to calculate the strain in real time from the images, it uses image processing algorithms that locate and follow the centres of the marks. This fact eliminates possible errors caused by marks elongation at high deformations as it happens during TPU testing. All the parameters from the tensile test and the results obtained were controlled by the commercial software BlueHill®.

2.4. Test conditions

Following the standard recommendations, five specimens were tested for each analysed configuration, thus a total of 20 specimens were tested. To avoid the effect of ageing, the time elapsed between the test and the manufacturing of the specimens was less than 24 hours. Moreover, on the first test day 4 specimens were tested, one for each analysed configuration. On the remaining test days, 4 specimens with the same configuration were tested each day.

The tests were carried out under displacement control with rate of 500 mm/min according to ISO 37 for tensile tests. Before starting the test, the load cell was tared and the initial distance between the marks on the specimens was measured using the video extensometer. During the test, the video extensometer was constantly measuring the distance between the marks. Once the test was completed, the obtained raw data were exported for further processing.

2.5. Classical hyperelastic models

The stress-strain curves can be used to calibrate hyperelastic models, i.e. adjusting the parameters of the models to fit the experimental results. The neo-Hookean, Ogden and Mooney-Rivlin models are used in this work.

2.5.1. Neo-Hookean

The first fitting model used was the neo-Hookean model [24]. The expression of the strain energy in hyperelastic materials according to this model is expressed in (1).

$$W_{neo-Hookean} = C_{10}(\bar{I}_1 - 3) \tag{1}$$

From (1), $\overline{I}_1$ is the first deformation invariant of the material. According to Bergstrom [24], when deriving this equation, the constant C_{10} represents the shear modulus of the material. So from now on, this variable will be referred as μ. Another characteristic of this model is that, as can be seen in (1), it has only one parameter. Thus, it will not correctly adjust the stress-strain curve for the entire deformation range of the analysed material, but it does provide a better adjustment than the Mooney-Rivlin [25, 26] and Ogden [27] models for the linear-elastic part. Therefore, this model has only been adjusted on this area.

2.5.2. Ogden model

The second fitting model used was the Ogden model [27]. This model has the characteristic of a good fit in elastomers and thermoplastics. The strain energy function in hyperelastic materials for this model is expressed in equation (2).

$$W_{Ogden} = \sum_{k=1}^{N} \frac{\mu_k}{\alpha_k} (\lambda_1^{\alpha_k} + \lambda_2^{\alpha_k} + \lambda_3^{\alpha_k} - 3) \tag{2}$$

In this equation $\lambda_1^{\alpha_k}$, $\lambda_2^{\alpha_k}$ y $\lambda_3^{\alpha_k}$ are the principal stretch ratios for the Ogden model. N is the number of terms selected to fit the material model, in this work a value of $N = 3$ was chosen. Finally, α_k and μ_k are parameters of the model.

2.5.3. Mooney-Rivlin model

The third and last fitting model used in this work was the second-order Mooney-Rivlin model [25, 26]. The general strain energy function of a hyperelastic material model for the Mooney-Rivlin model for five parameters (second order) is shown in equation (3).

$$\begin{aligned} W_{Mooney-Rivlin} = {} & C_{10}(\overline{I}_1 - 3) + C_{01} + (\overline{I}_2 - 3) + C_{11}(\overline{I}_1 - 3)(\overline{I}_2 - 3) \\ & + C_{20}(\overline{I}_1 - 3)^2 + C_{02}(\overline{I}_2 - 3)^2 + \frac{1}{d}(J - 1)^2 \end{aligned} \tag{3}$$

where $\overline{I}_1$ and $\overline{I}_2$ are the first and second invariant of the deformation respectively. C_{10}, C_{01}, C_{11}, C_{20} y C_{02} are material constants characterising the behaviour of the material during the test. d is the material incompressibility parameter. In the present study, it is set to 0.

3. Results

3.1. Tensile tests

Figure 4 shows the stress-strain curves for the four analysed configurations (changing the raster angle) and every tested specimen. Figure 5 exhibites a comparison of the stress-strain curves using a representative specimen for each analysed configuration, including two zoom areas on the initial linear-elastic zone and in the vicinity of 200% strain. Figure 6 shows an example of a broken specimen for each analysed configuration, including a global view and a detail of the fracture zone.

Figure 7 shows how some characteristic parameters were calculated. Figure 7a shows the calculation of Young's modulus. This parameter was obtained as the slope of the regression line formed by the initial points of the test that presented an axial deformation lower than 5% (0.05 mm/mm). This condition was set to ensure that a linear elastic zone was chosen for the Young's modulus evaluation. Other characteristic variables on hyperelastic materials are the strength values S100 and S300. The calculation of these parameters is shown in figure 7b. They were set by determining the axial stress at which deformations of 100% (1 mm/mm) and 300% (3 mm/mm) were reached. The values of these parameters for the 20 tested specimens are reported in table 3.

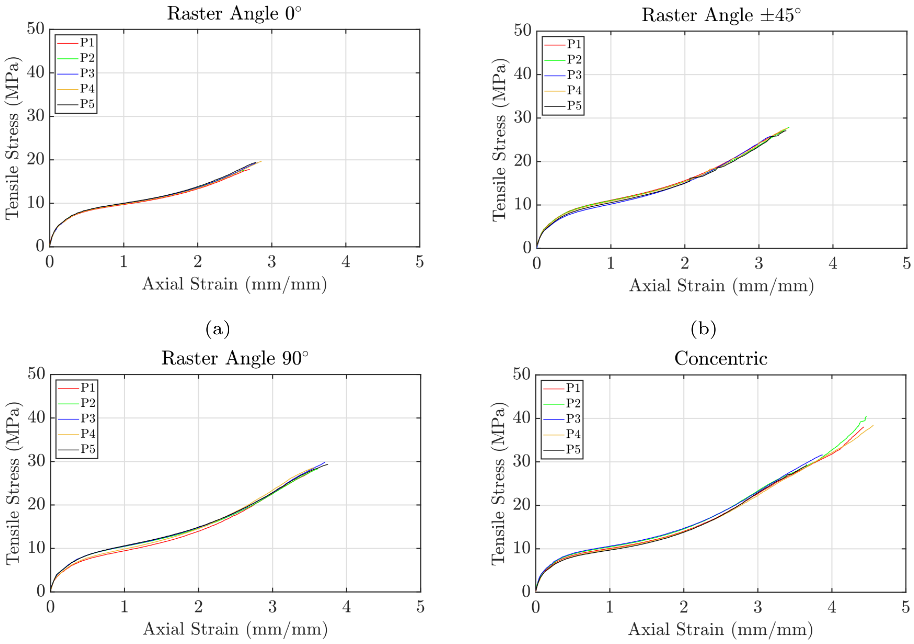

(a)

(b)

(c)

(d)

Figure 4: Stress-strain curves for the different analysed configurations.

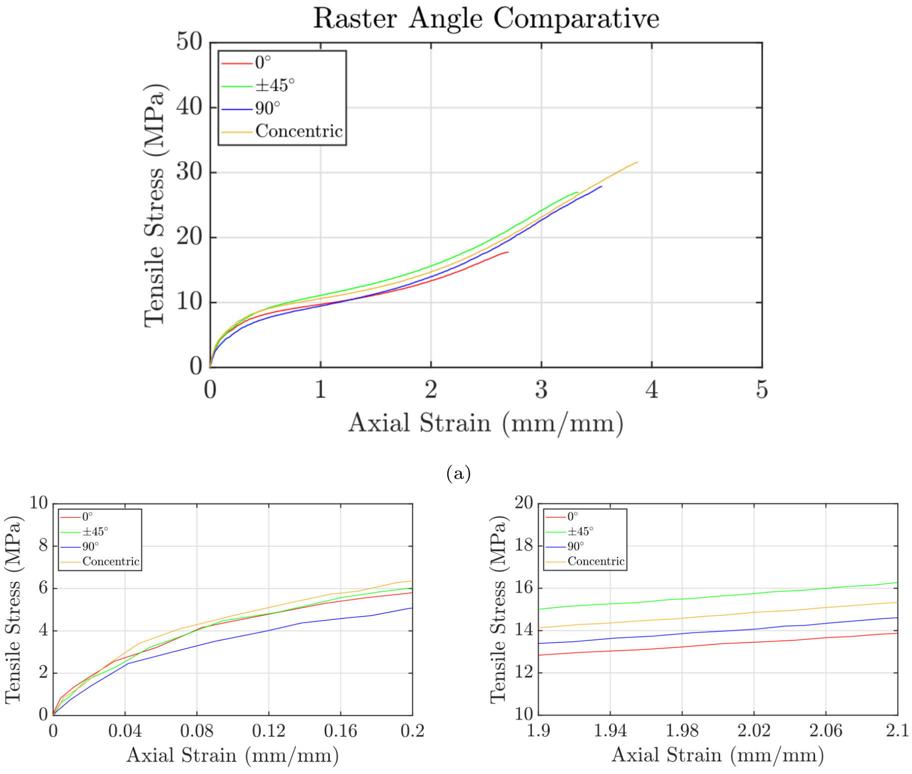

(a)

(b)

(c)

Figure 5: Comparison of a representative curve for each analysed configuration (a) global view, (b) zoom at the initial linear elastic zone and (c) zoom in the vicinity of 200% strain.

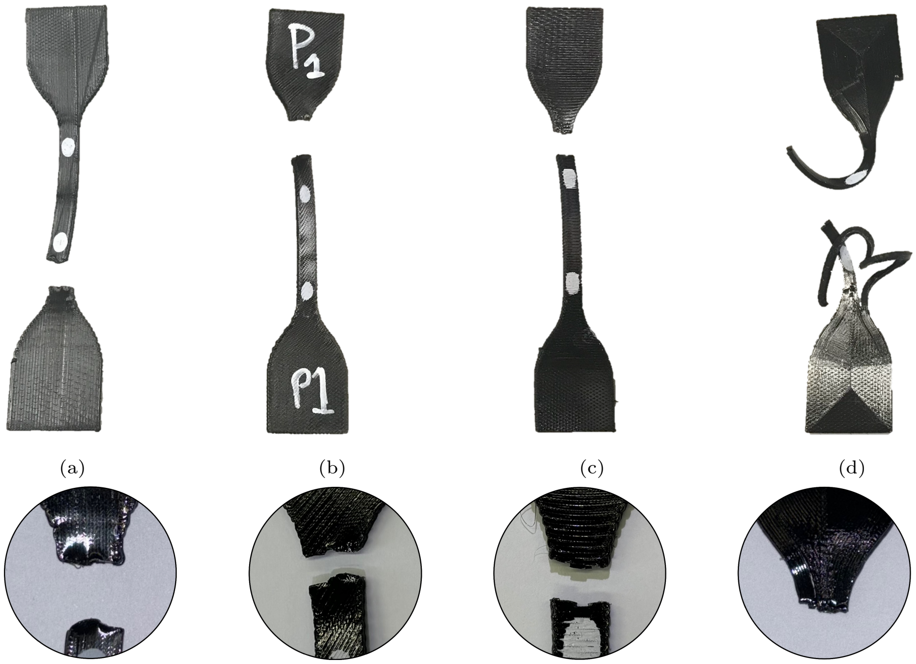

(a) (b) (c) (d)

(e) (f) (g) (h)

Figure 6: Example of a broken specimen for each analysed configuration. Global view for (a) 0°. (b) ±45°. (c) 90°. (d. Detail view of the fracture zone for (a) 0°. (b) ±45°. (c) 90°. (d) Concentric.

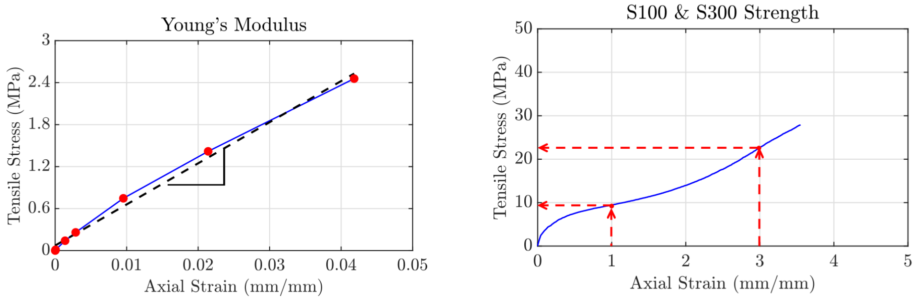

(a) (b)

Figure 7: Details of the calculation of the Young's modulus and S100 and S300 strength.

Specimen	S100 (MPa)	Mean S100 ±sd (MPa)	S300 (MPa)	Mean S300 ±sd (MPa)	Young's Modulus (MPa)	Mean Young's Modulus ±sd (MPa)	Mass (g)
0° P1	9.71	9.89 ±0.12	-	-	72.49	65.60 ±5.26	4.39
0° P2	9.96		-		63.01		4.53
0° P3	9.96		-		62.09		4.52
0° P4	9.83		-		60.51		4.53
0° P5	10.02		-		69.92		4.49
45° P1	11.10	10.74 ±0.38	24.15	24.32 ±0.75	66.98	63.14 ±4.13	4.48
45° P2	11.00		23.70		64.01		4.54
45° P3	10.20		24.24		66.37		4.53
45° P4	10.85		23.92		61.55		4.56
45° P5	10.54		25.61		56.81		4.49
90° P1	9.46	10.19 ±0.49	22.68	22.86 ±0.31	58.76	60.06 ±4.28	4.42
90° P2	10.46		22.56		60.30		4.37
90° P3	10.52		22.81		67.31		4.57
90° P4	9.90		23.38		57.10		4.57
90° P5	10.62		22.88		56.82		4.43
Conc. P1	10.08	10.14 ±0.38	22.67	22.86 ±0.42	68.14	70.69 ±6.38	4.38
Conc. P2	10.44		23.36		81.62		4.51
Conc. P3	10.60		23.14		70.58		4.58
Conc. P4	9.89		22.26		67.79		4.39
Conc. P5	9.69		22.87		65.33		4.37

Table 3: Young's modulus, S100 and S300 strength and mass for every tested specimen.

3.2. Fitting parameters for each hyperelastic model

3.2.1. Neo-Hookean

Table 4 shows μ values calculated for each configuration. This parameter was calculated by implementing in Matlab® R2024a a system of equations formed by equation (1) and the experimental data of the 5 manufactured specimens for each configuration. Additionally, this table also includes the average value of the root mean square error (RMSE) for the 5 specimens. Obtained results show that although the value of μ is of a similar order of magnitude for the different configurations, there are still differences between tested specimens.

Raster Angle (°)	Parameters μ (MPa)	RMSE (MPa)
0	22.984	0.228
±45	23.206	0.230
90	21.238	0.158
Concentric	25.573	0.236

Table 4: μ value obtained for the neo-Hookean model along the linear-elastic part for each analysed configuration and the root mean square error.

3.2.2. Ogden model

Table 5 shows the value of the six parameters obtained for each configuration, also the average value of RMSE is reported. The parameters were calculated solving a system of equations formed by equation (2) and the experimental data of the 5 manufactured specimens for each configuration, as done for the neo-Hookean model.

This table shows the effect of the raster angle on the obtained values for the six parameters of the Ogden model. For example, the parameter μ_1, for the specimens with a concentric and 0° pattern, shows a slightly higher absolute value than the rest of configurations. On the other hand, when analysing the obtained values for α_1, the specimens with a raster angle of 0° present the highest value, while the concentric specimens have the lowest value.

Raster	Parameters						RMSE
Angle (°)	μ_1 (MPa)	α_1	μ_2 (MPa)	α_2	μ_3 (MPa)	α_3	(MPa)
0	-16.361	3.602	4.171	-1.023	32.470	-7.226	0.197
±45	-13.901	2.353	2.099	-1.061	28.637	-4.739	0.312
90	-13.245	1.624	-4.86e-9	13.922	27.377	-3.441	0.381
Concentric	-15.699	1.620	-1.460	2.629	33.996	-3.730	0.498

Table 5: Ogden model obtained parameters for a N=3 for each configuration and the root mean square error.

3.2.3. Mooney-Rivlin model

Table 6 shows the value of the five parameters for each configuration. The parameters and the RMSE have been obtained in the same way as for the two previously described models. As in the case of the other fitting models, both the value of the different parameters and the RMSE are affected by the raster angle.

Raster	Parameters					RMSE
Angle (°)	C_{10} (MPa)	C_{01} (MPa)	C_{11} (MPa)	C_{20} (MPa)	C_{02} (MPa)	(MPa)
0	-15.913	25.449	0.203	-0.961	5.887	0.205
±45	-7.725	15.849	0.013	0.209	1.830	0.315
90	-2.821	9.874	-0.070	0.756	-0.481	0.387
Concentric	-6.646	14.928	-0.087	0.855	0.372	0.494

Table 6: Mooney-Rivlin model obtained parameters for each configuration and the root mean square error.

3.3. Obtained stress-strain curves using the fitted hyperelastic models.

Figure 8 shows the comparison of the 3 analysed fitting models with the experimental data in the linear-elastic part of the curves for the different analysed configurations. Additionally, figure 9 shows the fitting for the whole stress-strain curve of the Mooney-Rivlin and the Ogden models only. As already mentioned, the curve obtained by the neo-Hookean model has not been added, because the use of only one parameter did not correctly adjust the double curvature of hyperelastic behaviour.

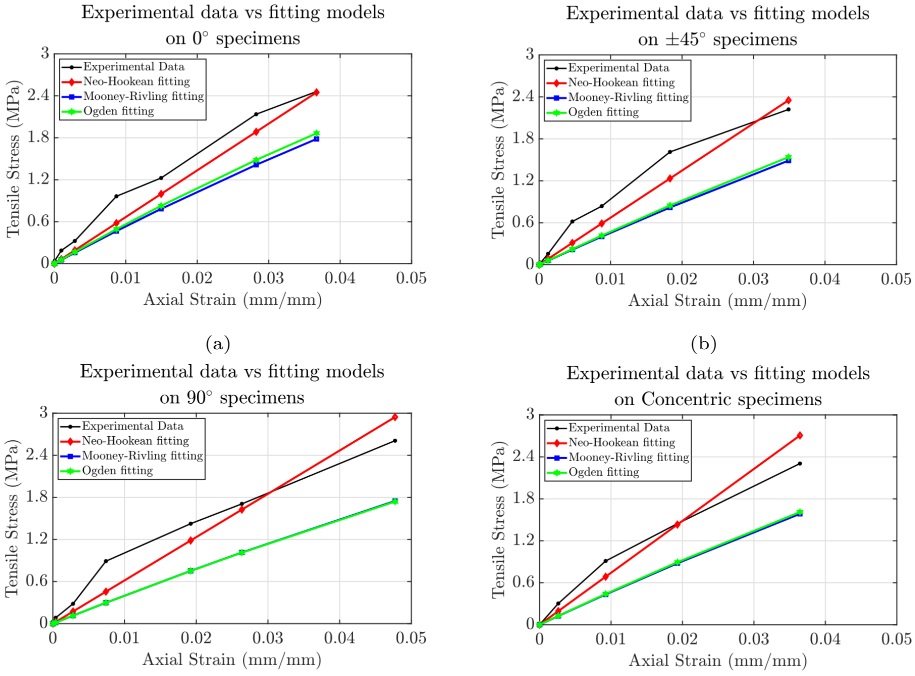

(a) (b)

(c) (d)

Figure 8: Comparison of the 3 fitting models and the experimental data on the linear-elastic part for the different tested configurations.

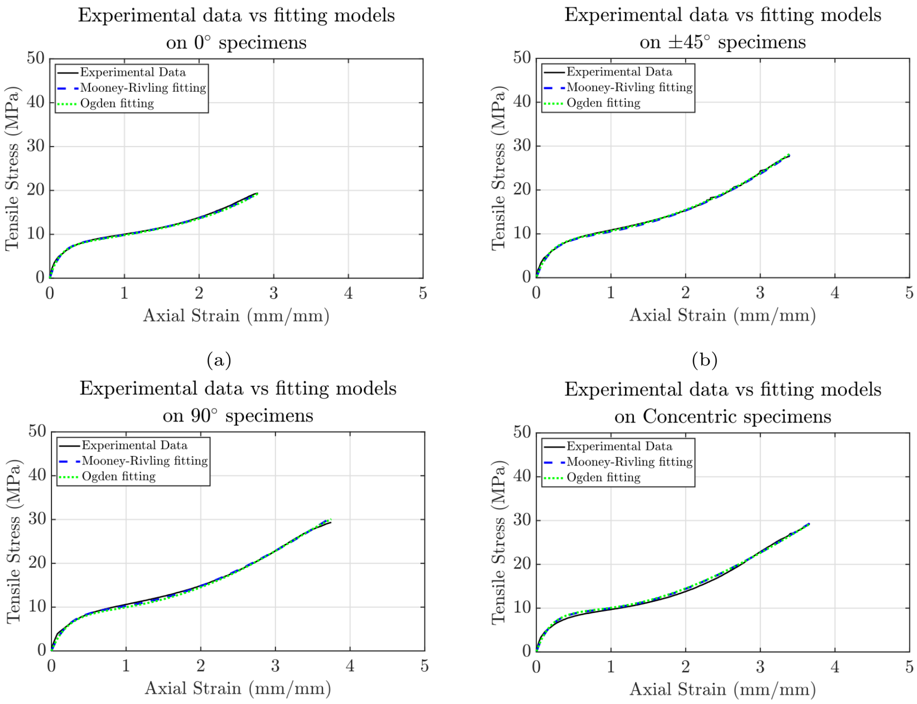

(a) (b)

(c) (d)

Figure 9: Comparison of the experimental data, the Mooney-Rivlin and the Ogden models for each analysed configuration.

4. Discussion

4.1. Stress-strain curves

Figures 4 and 5 show that the obtained stress-strain plots present the traditional shape for tensile testing of hyperelastic materials [10] for all the analysed infill configurations. The curves show two changes of slope, one at a low strain value and the other change occurs once the 200% strain is exceeded. Similarly, this curve shows two highly differentiable parts. One part corresponds to the first stage of the test in which the material showed a linear elastic behaviour. That is why, this first stage of the stress-strain curve was used for the calculation of Young's modulus. This zone is between the beginning of the test and 5-6% of the axial strain, where the first change of slope in the curve occurs. The second stage presented by the material in the tensile test began precisely with the change of slope and the end of the linear stage, covers the second change of slope of the curve and ended with the specimen breakage. This part showed a highly non-linear stress-strain relationship, which corresponds to the viscoelastic behaviour of the material [10].

The analysis of the S100 and S300 values included in table 3 for each group of specimens showed a high repeatability of the results. Results for Young's modulus were more disperse between specimens in the same group. This behaviour may be due to the small amount of data (due to the high speed used during the test) during the linear-elastic part of these specimens (less than 7 points).Analysing together the results presented in figures 4, 5 and 6 and the table 3, several conclusions can be reached related to the effect of the raster angle on the behaviour of tested specimens. The first conclusion is that the specimens at 0° are the ones with the lowest tensile strength, which is confirmed in the table 3, as these specimens do not even reach a deformation of 3 mm/mm (S300) (Figure 5), despite being the second group of specimens with the highest Young's modulus. This behaviour could be explained by the stress raisers induced by the printing procedure, see figure 2a. It can be seen that in the zone close to the rounded area of the specimen, the different filament endings create corners which accelerates the specimen breakage. It should be noted that these stress raisers (or sawtooth shape in the printing pattern) are associated to the fact that all the filaments are forced to be oriented at 0°. The specimens with a concentric infill are on the opposite side. As these specimens do not have any type of sawtooth-shaped area in their profile, they presented both ultimate stress and strain values much higher than the other configurations, with some of these specimens presenting strain values larger than 4 mm/mm. Moreover, these specimens showed a peculiar fracture behaviour, since, as can be seen in figure 6d, the breakage was produced by tearing one of the outermost filaments of the specimen, showing a curling of this filament as well as a debonding between printed filaments.

The highest S100 and S300 values were reported for specimens manufactured with a raster angle of ±45° (Figure 5). This behaviour may be related to the fact that these specimens are the only ones that present a cross-ply configuration between the different printing layers of the specimen, leading to a less anisotropic behaviour than the other configurations. Nevertheless, both its ultimate stress and strain were higher than the 0° configuration only.

Finally, the 90° specimens were the ones with the lowest Young's modulus. However, they have large values of ultimate stress and strain, only behind the specimens with a concentric infill pattern. The explanation for this behaviour may be associated to the way these specimens deform and break during the tensile test (Figure 6c). During the tensile test, elongation of 90° specimens is associated to a transversal deformation of the printed filaments. This fact is directly related to a lower Young's modulus and obtained large strains. Moreover, obtained high strength is directly related to a very good bonding between printed filaments. It is interesting to recall, that the fracture surface is not a plane (as it may be expected) but a stepped surface (coinciding with printing layers) is always obtained, see (Figure 6c). From this discussion is possible to conclude that the raster angle affects the mechanical properties, as can be clearly seen from the values reported in table 3, showing an average difference of ∼10 MPa (∼15%) between the Young's modulus of the specimens with a raster angle of 90° and the concentric pattern specimens. The effect of the raster angle can also be seen in the S300 value where, for example, the specimens manufactured at 0° do not even reach this value. Another mechanical property that was also affected by the raster angle was the ultimate stress and strain. Figure 4 shows that almost every concentric pattern specimen break with a strain value higher than 400% and with a stress close to 40 MPa, while the specimens at 0° hardly reach to 20 MPa at break.

4.2. Fitting hyperelastic models

According to the values obtained in table 4 for the neo-Hookean model and the comments made by Bergstrom [24] in their work, the raster angles with the highest shear modulus are the specimens with a concentric pattern and the specimens with a raster angle of ±45°. On the other hand, the configuration with the lowest shear modulus was 90°. This fact could also be associated to the printed filament direction which is perpendicular to the load in that configuration.

As could be seen in parameters of the Ogden model in the table 5, the most noteworthy case is the 90° configuration. For this type of specimens, the value of μ_2 was close to zero, much lower in absolute value than the same parameter for the rest of the specimens, which caused the value of α_2 to be positive and an order of magnitude higher than that of the rest of the specimens. Likewise, the same parameter for the specimens with a concentric infill pattern presented negative values and, as a consequence, negative α_2 values, which was an opposite result to the 0° and ±45° configurations.

For this model, the RMSE value increases as the raster angle increases, with the specimens with a concentric infill having the highest values.

Mooney-Rivlin model parameters shown in table 6 allowed further discussion of the raster angle effect, since, they presented different values for each type of specimen. This behaviour also affected the RMSE. Recalling RMSE, its behaviour may be expected, as the lowest RMSE values were obtained for the specimens with the filaments oriented at 0°, which present the lowest ultimate strain (i.e. shortest curves), see table 3 and figure 4. From a fitting point of view, shorter curves allow an easier adjustment. On the other hand, the specimens with a concentric filament orientation had the highest RMSE values. Once again, this behaviour could be related the highest ultimate strains, thus fitting this curve could be slightly more complicated.

Regarding figure 8, it reflects how the neo-Hookean model is the one that best fits the experimental results, in the linear-elastic zone, for every analysed configuration. Regarding the Mooney-Rivlin model and the Ogden model, two remarkable behaviours can be appreciated (see figure 9), the first one is that both models perform a very close fitting to the experimental data. The second is that both models show very similar results. This can be expected, due to the fact that the RMSE values in tables 5 and 6 were very similar for both models.

5. Conclusions

The first aim of this work was to analyse the raster angle effect on the mechanical properties of additive manufactured parts using an hyperelastic material. For this purpose, TPU specimens were manufactured using line infill patterns and 100% infill density. This selection was done in order to avoid any other variable that may also have an effect on the mechanical behaviour. The analysed configurations were 0°, ±45°, 90° and concentric pattern. A uniaxial tensile test was performed on each specimen and the effect that the raster angles had on different mechanical parameters such as Young's modulus, ultimate stress and strain or the way the specimens broke was analysed.

In addition, 3 fitting models widely used in the literature(i.e. neo-Hookean, Ogden and Mooney-Rivlin) have been used to analyse their performance when fitting a 3D printed hyperelastic part and whether, again, the different raster angles had effects on the parameters needed to fit these models.

Regarding the experimental campaign, it can be concluded that the raster angle has an effect on the different variables derived from the tensile test. Among the results obtained, the specimens with a raster angle of ±45° were the ones with the highest S100 and S300 values, which may be associated to the cross-ply configuration among the printed layers. The specimens with a concentric infill pattern were those with the highest ultimate stress and strain. The disposition of the filaments favoured a higher tensile strength, due to the fact that the filaments were elongated in the printing direction. On the other hand, the specimens with a raster angle of 0° were the ones that supported the least strain and stress values. This behaviour is associated to the presence of stress raisers (sawtooth profile / corners) in the rounded part of the specimens caused by the ending of several printed filaments. Finally, 90° specimens were those with the lowest Young's modulus, this behaviour was once again associated to the disposition of the filaments and the loading direction during the tensile test, i.e. printed filaments were elongated in their transverse direction.

Thus, obtained results confirm the anisotropic hyperelastic behaviour of 3D printed TPU parts which should be taken into account from a design point of view. Finally, concerning the fitting models, there was evidence that the neo-Hookean model was the one that best fitted the curves in the elastic-linear zone, while once this zone was exceeded, it made no sense to use it. Both the Mooney-Rivlin and Ogden models presented similar fits to the experimental data, even obtaining a very similar RMSE value between models for each analysed configuration. It will be interesting to analyse other types of tests, such as plane stress or biaxial stress tests, and verify wheter these models will show similar behaviour between them or not, this study being considered as a future work.

Conflict of interest

On behalf of all authors, the corresponding author states that there is no conflict of interest.

References

[1] Nazir A., Gokcekaya O., Md Masum Billah K., Ertugrul O., Jiang J., Sun J., Hussain S. Multi-material additive manufacturing: A systematic review of design, properties, applications, challenges, and 3D printing of materials and cellular metamaterials (2023) Materials and Design, 226, 111661.

[2] Wang X., Jiang M., Zhou Z., Gou J., Hui D. 3D printing of polymer matrix composites: A review and prospective (2017) Composites Part B: Engineering, 110, 442-458.

[3] Kabir S.M.F., Mathur K., Seyam A.-F.M., A critical review on 3D printed continuous fiber-reinforced composites: History, mechanism, materials and properties (2020) Composite Structures, 232, 111476.

[4] Rajan K., Samykano M., Kadirgama K., Sharuzi W., Rahman M., Fused deposition modeling: process, materials, parameters, properties, and applications (2022) The International Journal of Advanced Manufacturing Technology, 120, 1531-1570.

[5] Sha L., Chen Z., Chen Z., Zhang A., Yang Z. Polylactic acid based nanocomposites: promising safe and biodegradable materials in biomedical field (2016) International Journal of Polymer Science, 9, 1–11.

[6] Elmrabet N., Siegkas P. Dimensional considerations on the mechanical properties of 3D printed polymer parts (2020) Polymer Testing, 90, 106656.

[7] Tao Y., Shao J., Li P., Shi S.Q. Application of a thermoplastic polyurathane/polylactic acid composite filament for 3D-printed personalized orthosis (2019) Materials and Technologies, 53 (1) 71–76.

[8] de Leon A.C., Chen Q., Palaganas N.B., Palaganas J.O., Manapat J., Advincula R.C. High performance polymer nanocomposites for additive manufacturing applications (2016) Reactive and Functional Polymers, 103, 141–155.

[9] Hohimer C., Christ J., Aliheidari N., Mo C., Ameli A. 3D printed thermoplastic polyurethane with isotropic material properties (2018) Conference Paper.

[10] Boubakri A., Haddar N., Elleuch K., Bienvenu Y. Impact of aging conditions on mechanical properties of thermoplastic polyurethane (2010) Materials and Design, 31, 4194 – 4201.

[11] Nace S.E., Tiernan J., Holland D., Ni Annaidh A. A comparative analysis of the compression characteristics of a thermoplastic polyurethane 3D printed in four infill patterns for comfort applications (2021) Rapid Prototyping Journal, 27 (11), 24 - 36.

[12] Xiao J., Gao Y. The manufacture of 3D printing of medical grade TPU (2017) Progress in Additive Manufacturing, 2 (3), 117 - 123.

[13] Bruère V.M., Lion A., Holtmannspötter J., Johlitz M.The influence of printing parameters on the mechanical properties of 3D printed TPU-based elastomers (2023) Progress in Additive Manufacturing, 8 (4), 693 - 701.

[14] Dilibal S., Sahin H., Celik Y. Experimental and numerical analysis on the bending response of the geometrically gradient soft robotics actuator (2018) Archives of Mechanics, 70 (5), 391 - 404.

[15] Raj G.B., Saludheen A., Arumugham-Achari A.K., George N., Chacko T. Simulations for mechanical properties of polymer composites: investigations into suitability of numerical models for TPU-CNT with Mooney–Rivlin (N= 1) and friction (2023) Mechanics of Time-Dependent Materials, 27 (3), 705 - 726.

[16] Viccica M., Giordano M., Galati M., Additive manufacturing of flexible thermoplastic polyurethane (TPU): enhancing the material elongation through process optimisation (2024) Progress in Additive Manufacturing. https://doi.org/10.1007/s40964-024-00790-y

[17] Domínguez-Robles J., Utomo E., Cornelius V.A., Anjani Q.K., Korelidou A, Gonzalez Z, Donnelly R.F., Margariti A., Delgado-Aguilar M., Tarrés Q., Larrañeta E. TPU-based antiplatelet cardiovascular prostheses prepared using fused deposition modelling (2022) Materials & Design 220, 110837.

[18] Jaradat M., Soliman E., Taha M.R. 3D-printed bio-inspired mechanically interlocked viscoelastic dampers for energy dissipation (2023) Materials & Design 228, 111826.

[19] Zhuo Z., Ouyangb Y., Zheng X., Chen X., Lin Z., Zhud R., Lana L., Qiana D., Lic R., Zhu J., Dang Y., Wang Y., Liao S., Tian X., Yang F. Design, fabrication, and in vitro studies of sustained paclitaxel release from 3D-printed TPU/P407 airway stents for treating airway stenosis (2024) Materials & Design 245, 113252

[20] Lin T.A., Limin B., Lin M-C. Lin J-Y., Lou C-W., Lin J-H., Impact-resistant polypropylene/thermoplastic polyurethane blends: compatible effects of maleic anhydride on thermal degradation properties and crystallization behaviors (2019) Journal of Materials Research and Technology 8(4) 3389–3398.

[21] Rahmatabadi D., Ghasemi I., Baniassadi M., Abrinia K., Baghani M. 3D printing of PLA-TPU with different component ratios: Fracture toughness, mechanical properties, and morphology (2022) Journal of Materials Research and Technology 21:3970-3981.

[22] Arifvianto B., Satiti B.E. Salim U.A., Suyitno, Nuryanti A., Mahardika M., Mechanical properties of the FFF sandwich-structured parts made of PLA/TPU multi-material (2022) Progress in Additive Manufacturing 7:1213–1223.

[23] Abad F., Lotfian S., Dai S., Zhao G., Alarcon G.I., Yang L., Huang Y., Xiao Q., Brennan F. Experimental and computational analysis of elastomer membranes used in oscillating water column WECs (2024) Renewable Energy, 226, art. no. 120422

[24] Bergström J. Mechanics of Solid Polymers: Theory and Computational Modeling (2015) Mechanics of Solid Polymers: Theory and Computational Modeling, 1 - 509.

[25] Mooney, M. A Theory of Large Elastic Deformation (1940) Journal of Applied Physics, 11(9), 582–592.

[26] Rivlin R.S. Large Elastic Deformations of Isotropic Materials. I. Fundamental Concepts (1997) In: Barenblatt G.I., Joseph D.D. (eds) Collected Papers of R.S. Rivlin. Springer, New York, NY

[27] Ogden, R.W. Non-linear elastic deformations (1997) Second Edition. New York.: Dover Publications.

[28] Távara L., Madrigal C., Aranda M.T., Justo, J. Anisotropy and ageing effect on the mechanical behaviour of 3D-printed short carbon-fibre composite parts (2023) Composite Structures, 321, 117196.

[29] Estefani A., Távara L. Numerical multiscale analysis of 3D printed short fiber composites parts: Filament anisotropy and toolpath effects (2024) Engineering Reports, 6 (7), art. no. e12799

[30] Smart Materials 3D. Technical Data Shet FLEX 93A v. 1.2 (2023).